NORGES TEKNISK-NATURVITENSKAPELIGE
UNIVERSITET

Bayesian AVO Inversion

by

Arild Buland and Henning Omre

PREPRINT
STATISTICS NO. 5/2001
ISSN: 0804-9173

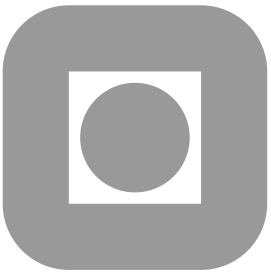

NORWEGIAN UNIVERSITY OF SCIENCE AND
TECHNOLOGY
TRONDHEIM, NORWAY

This report has URL http://www.math.ntnu.no/preprint/statistics/2001/S5-2001.ps
Arild Buland has homepage: http://www.math.ntnu.no/~arildbu
E-mail: arildbu@math.ntnu.no
Address: Department of Mathematical Sciences, Norwegian University of Science and Technology,
N-7491 Trondheim, Norway.

Bayesian AVO inversion

Arild Buland* and **Henning Omre†**
(October 26, 2000)

ABSTRACT

A Bayesian AVO inversion technique is developed where the solution is given as a posterior distribution for the inverted model parameters. The uncertainty in the inverted parameters is an integrated part of the solution. The inversion algorithm is based on a time continuous weak contrast model. The model parameters are represented by temporal log-Gaussian fields, and derivative Gaussian fields are involved to couple the absolute values of the parameters to the contrast model needed in the reflectivity calculation. The solution of the AVO inversion is given in an analytical form. The inversion algorithm is fast and has been tested on synthetic gathers and a real 3-D dataset from the Sleipner Field.

*Statoil Research Centre, Postuttak, N-7005 Trondheim, Norway,
and
Norwegian University of Science and Technology, N-7491 Trondheim, Norway.
†Norwegian University of Science and Technology, N-7491 Trondheim, Norway.

INTRODUCTION

The objective of geophysical inverse problems is to make inferences about model parameters based on general knowledge and a set of geophysical measurements. In general, these inverse problems are multidimensional and ill-posed, and they are often strongly affected by noise and measurement uncertainty. Two important problems related to an ill-posed inverse problem are that it may not have any solutions, which is typical for an over determined problem, or a possible solution may not be unique, which is typical for under determined problems. Non-uniqueness means that several models fit the measured data equally well. The earth parameters vary in three spatial directions, leading to an infinite dimensional problem. In a realistic exploration situation, only a limited amount of data are available, making the inverse problem inherently non-unique. Another aspect of non-uniqueness is related to identifiability of the parameters from the data. This problem arise when more than one parameter set have the same forward response. Further, an ill-posed problem may be unstable, that means that the solution is highly sensitive to slight perturbations in the data.

In a statistical perspective, the solution of an inverse problem is not limited to a single set of predicted parameters, but is represented by a probability density function (pdf) on the model space. The aim of inversion is not only to find a best-fitting set of model parameters, but also to characterize the uncertainty in the inversion results. A Bayesian setting is a natural choice for many geophysical inverse problems, where it is possible to combine available prior knowledge with the information contained in the measured data (Tarantola and Valette, 1982a; Tarantola, 1987; Duijndam, 1988a; Duijndam, 1988b,). The solution of a Bayesian inverse problem is represented by the posterior (aposteriori) distribution. Analysis of non-uniqueness and uncertainty in the solutions of inverse problems are often called resolution analysis. In a Bayesian setting, all questions about resolution are addressed by the posterior distribution.

The general geophysical inverse problem has a non-linear relationship between the model parameters and the measured data, and the posterior distribution can only be found by use of stochastic simulation techniques (Monte Carlo) (Mosegaard and Tarantola, 1995; Sen and Stoffa, 1996; Mosegaard, 1998; Eide et al., 1999,). However, stochastic simulation of inverse problems involving seismic data are in most cases unpractical due to a high computional cost. For linear problems, or problems which can be linearized, analytical solutions may be found.

AVO inversion is a seismic prestack inversion technique which can be used to estimate elastic subsurface parameters (Hampson and Russell, 1990; Dahl and Ursin, 1991; Buland et al., 1996,). The reflection strength from subsurface interfaces depends directly on the material properties where the reflections take place, and on the reflection angle. This amplitude versus angle (AVA) dependency, or amplitude versus offset (AVO), is the fundament for this kind of inversion. Seismic prestack data also contain information on porosity, lithology and pore fluid, and AVO inversion can also be used to extract information on these properties. However, estimation of these properties from seismic data is a highly non-unique problem, and uncertainty estimates given by the posterior distribution are therefore a necessary and important part of the solution.

In this paper, a Bayesian linearized AVO inversion method is presented, where the objective is to obtain posterior distributions for the absolute values of P-wave velocity, S-wave velocity and density, but the distributions for other elastic parameters can also be predicted. A Bayesian approach to linearized AVO inversion was also used by (Lörtzer and Berkhout, 1993), but they formulated the inversion algorithm for relative contrasts instead of absolute values. Further, they used standard AVO techniques based on single interface theory, which are then applied independently on a sample for sample basis. We have based the inversion algorithm on a time continuous weak contrast model. The model parameters are represented by temporal log-Gaussian fields, and derivative Gaussian fields are involved to couple the absolute values of the parameters to the contrast model needed in the reflectivity calculation. The inversion is based on prior information and true amplitude processed seismic prestack data. Important steps in the processing are removal of multiples, the effect of geometrical spreading and the effect of absorption. We further assume that wave mode conversions, interbed multiples and anisotropy effects can be neglected after processing. The data should be prestack migrated, such that each single bin-gather can be regarded as the response of a local 1-D earth model. The prestack migration implicitly NMO corrects the data. Finally, the gathers must be transformed from offsets to angles, either by common-angle migration, or by a transform after the migration. The processed data are represented by convolution of the primary reflectivity with a source wavelet plus an error term, which includes all kind of noise in the raw data and all kinds of processing artifacts.

In the following sections the methodology, synthetic tests and the application of the inversion method on a real 3-D dataset are presented.

METHODOLOGY

The seismic reflectivity depends on the material properties of the subsurface. An isotropic, elastic medium is completely described by three material parameters. We have chosen $\{\alpha(t), \beta(t), \rho(t)\}$, where $\alpha(t)$, $\beta(t)$ and $\rho(t)$ are P-wave velocity, S-wave velocity and density, but several other parameterizations can also be used, for example $\{\lambda(t), \mu(t), \rho(t)\}$, where λ and μ are the Lamé param-

eters. The relationship between these two parameter sets are given by $\alpha = \sqrt{(\lambda + 2\mu)/\rho}$ and $\beta = \sqrt{\mu/\rho}$. The material properties can also be described by impedances, $\{Z_P(t), Z_S(t), \rho(t)\}$, where $Z_P = \alpha\rho$ is the acoustic impedance, and $Z_S = \beta\rho$ is the shear impedance. The shear impedance is often substituted by the P-wave velocity to S-wave velocity ratio α/β. However, the parameterization is not important if the possible dependencies between the different parameters are included in the model. When inversion results are obtained for a chosen parameter set, the corresponding results can easily be calculated for another parameter set, including uncertainty.

The inversion method is based on a weak contrast approximation to the seismic reflectivity (Aki and Richards, 1980,):

$$c_{PP}(\bar{\theta}) \approx a_\alpha(\bar{\theta})\frac{\Delta\alpha}{\bar{\alpha}} + a_\beta(\bar{\theta})\frac{\Delta\beta}{\bar{\beta}} + a_\rho(\bar{\theta})\frac{\Delta\rho}{\bar{\rho}}, \tag{1}$$

where

$$a_\alpha(\bar{\theta}) = \frac{1}{2}\left(1 + \tan^2\bar{\theta}\right), \tag{2}$$

$$a_\beta(\bar{\theta}) = -4\frac{\bar{\beta}^2}{\bar{\alpha}^2}\sin^2\bar{\theta}, \tag{3}$$

$$a_\rho(\bar{\theta}) = \frac{1}{2}\left(1 - 4\frac{\bar{\beta}^2}{\bar{\alpha}^2}\sin^2\bar{\theta}\right), \tag{4}$$

and $\bar{\alpha}$, $\bar{\beta}$ and $\bar{\rho}$ are average P-wave velocity, S-wave velocity and density over the reflecting interface, $\Delta\alpha$, $\Delta\beta$ and $\Delta\rho$ are the corresponding (weak) contrasts, and $\bar{\theta}$ is average angle relative to the interface normal. Expressions on a similar form also exist for c_{PS}, c_{SP}, and c_{SS}. For simplicity, only PP reflectivity is discussed in this paper, but the extension to include converted waves are straightforward.

In the following, a continuous analog of the relative contrast terms $\frac{\Delta\alpha}{\bar{\alpha}}$, $\frac{\Delta\beta}{\bar{\beta}}$ and $\frac{\Delta\rho}{\bar{\rho}}$ will be used:

$$\frac{\Delta\alpha}{\bar{\alpha}} \rightarrow \frac{\partial}{\partial t}\ln\alpha(t) = \alpha'_L(t), \tag{5}$$

$$\frac{\Delta\beta}{\bar{\beta}} \rightarrow \frac{\partial}{\partial t}\ln\beta(t) = \beta'_L(t), \tag{6}$$

$$\frac{\Delta\rho}{\bar{\rho}} \rightarrow \frac{\partial}{\partial t}\ln\rho(t) = \rho'_L(t). \tag{7}$$

The time continuous analog of the reflection coefficient in equation (1) can be written

$$c_{PP}(t,\theta) \approx a_\alpha(t,\theta)\,\alpha'_L(t) + a_\beta(t,\theta)\,\beta'_L(t) + a_\rho(t,\theta)\,\rho'_L(t). \tag{8}$$

We now assume that the coefficients $a_\alpha(t,\theta)$, $a_\beta(t,\theta)$ and $a_\rho(t,\theta)$ can be represented by a constant or slowly varying background model, while the perturbations $\alpha'_L(t)$, $\beta'_L(t)$ and $\rho'_L(t)$ give the main contribution to the reflectivity. The approximation of the reflection coefficient will then separate into a pure angle dependent and a pure time dependent function

$$c_{PP}(t,\theta) \approx [\bar{a}_\alpha(\theta), \bar{a}_\beta(\theta), \bar{a}_\rho(\theta)] \begin{bmatrix} \alpha'_L(t) \\ \beta'_L(t) \\ \rho'_L(t) \end{bmatrix} = \bar{\boldsymbol{a}}^T(\theta)\,\boldsymbol{m}'_L(t), \tag{9}$$

where the bar on the a-coefficients indicates that they are based on a constant or slowly varying background model. If the background model is slowly varying, the coefficients are still time dependent, but we include this slowly varying effect into the interpretation of the bar symbol. The inversion algorithm requires that the background model must be known prior to the inversion, such that the coefficients $\bar{a}_\alpha(\theta)$, $\bar{a}_\beta(\theta)$ and $\bar{a}_\rho(\theta)$ can be precalculated.

In the formulas above, the reflection angle θ is used as an independent variable, but the seismic data are not directly recorded as function of reflection angle, but as function of source-receiver distance h (offset). The transform of the data from the (t,h)-domain to the (t,θ)-domain depends on the velocity function. This transform can be performed by angle-migration, ray-tracing or standard approximative offset-angle relations usually based on a smooth velocity function (the prior known background model).

The prior model

The prior model defines a statistical model for the prior information of the material parameters, expressed mathematically by a probability density function (pdf). The prior information must be independent of the seismic data, and is established from other available information and knowledge.

The inhomogeneous material parameters are collected in a vector field

$$\boldsymbol{m}(t) = [\alpha(t), \beta(t), \rho(t)]^T, \tag{10}$$

which is a priori modeled as a log-Gaussian random field, which implies that the elements in $\boldsymbol{m}(t)$ are restricted to take positive values. The logarithm of the material parameters then defines a Gaussian vector field

$$\boldsymbol{m}_L(t) = [\ln\alpha(t), \ln\beta(t), \ln\rho(t)]^T \sim \mathcal{N}_3(\boldsymbol{\mu}(t), \boldsymbol{\Sigma}(t,t')), \tag{11}$$

with a constant or slowly varying expectation

$$\boldsymbol{\mu}(t) = [\mu_\alpha(t), \mu_\beta(t), \mu_\rho(t)]^T, \tag{12}$$

and covariance function

$$\boldsymbol{\Sigma}(t,t') = \boldsymbol{\Sigma}_0(t)\rho_S(t,t'), \tag{13}$$

where $\mathbf{\Sigma}_0(t)$ is a covariance matrix between the elements $\ln\alpha(t)$, $\ln\beta(t)$, and $\ln\rho(t)$, and $\rho_S(t,t')$ is a spatial (temporal) correlation function. The correlation function must be positive definite, take values in the interval $[-1,1]$, and have the property that $\rho_S(t,t) = 1$. The diagonal elements of $\mathbf{\Sigma}_0(t)$ are the variances of $\ln\alpha(t)$, $\ln\beta(t)$, and $\ln\rho(t)$, denoted $\sigma^2_\alpha(t)$, $\sigma^2_\beta(t)$ and $\sigma^2_\rho(t)$.

The time derivative of the logarithm of the material parameters defines a new vector field

$$\boldsymbol{m}'_L(t) = [\partial_t \ln\alpha(t), \partial_t \ln\beta(t), \partial_t \ln\rho(t)]^T, \tag{14}$$

where the notation $\partial_t = \frac{\partial}{\partial_t}$ is used. This is also a Gaussian random field due to the linearity of the differentiation process (Christakos, 1992,):

$$\boldsymbol{m}'_L(t) \sim \mathcal{N}_3(\partial_t \boldsymbol{\mu}(t), \partial_t\partial_{t'}\mathbf{\Sigma}(t,t')). \tag{15}$$

For simplicity, we now assume that $\mathbf{\Sigma}(t,t')$ is stationary, such that $\mathbf{\Sigma}_0(t) = \mathbf{\Sigma}_0$, and $\rho_S(t,t') = \rho_S(\tau)$, where $\tau = |t-t'|$ is the time-lag. An example on a valid differentiable stationary correlation function is the second order exponential function

$$\rho_S(\tau) = \exp\left[-\left(\frac{\tau}{d}\right)^2\right], \tag{16}$$

where d is a range parameter characterizing the smoothness or the typical layer thickness of the target zone. In this case, $\partial_t\partial_{t'}\mathbf{\Sigma}(t,t') = -\mathbf{\Sigma}_0\partial^2_\tau\rho_S(\tau)$, see (Abrahamsen, 1997). Note further that $\mathrm{Cov}\{\boldsymbol{m}_L(t), \boldsymbol{m}'_L(t)\} = \mathbf{\Sigma}_0\partial_\tau\rho_S(\tau)$.

A discrete representation of $\boldsymbol{m}(t)$ in a given time interval is

$$\boldsymbol{m} = [\boldsymbol{\alpha}^T, \boldsymbol{\beta}^T, \boldsymbol{\rho}^T]^T, \tag{17}$$

which is multi-log-Gaussian. A discrete representation of $\boldsymbol{m}_L(t)$ will be multi-Gaussian:

$$\boldsymbol{m}_L = [\ln\boldsymbol{\alpha}^T, \ln\boldsymbol{\beta}^T, \ln\boldsymbol{\rho}^T]^T \sim \mathcal{N}_{n_m}(\boldsymbol{\mu}_{m_L}, \mathbf{\Sigma}_{m_L}), \tag{18}$$

where n_m is the dimension of $\boldsymbol{m}_L$ (and $\boldsymbol{m}$), and $\boldsymbol{\mu}_{m_L}$ and $\mathbf{\Sigma}_{m_L}$ are defined by the continuous analogs $\boldsymbol{\mu}(t)$ and $\mathbf{\Sigma}_0\rho_S(\tau)$, respectively. A discrete representation of $\boldsymbol{m}'_L(t)$ in a time interval is multi-Gaussian:

$$\boldsymbol{m}'_L = [\boldsymbol{\alpha}'^T_L, \boldsymbol{\beta}'^T_L, \boldsymbol{\rho}'^T_L]^T \sim \mathcal{N}_{n_m}(\boldsymbol{\mu}_{m'_L}, \mathbf{\Sigma}_{m'_L}), \tag{19}$$

with $\boldsymbol{\mu}_{m'_L}$ and $\mathbf{\Sigma}_{m'_L}$ being defined from $\partial_t\boldsymbol{\mu}(t)$ and $-\mathbf{\Sigma}_0\partial^2_\tau\rho_S(\tau)$, respectively.

If the target zone for the inversion contains some major changes in the subsurface, the weak contrast assumption is not valid. A possible solution may be to define the model as a stack of inhomogeneous layers

$$\boldsymbol{m} = [\boldsymbol{\alpha}^T_1, \ldots, \boldsymbol{\alpha}^T_l, \boldsymbol{\beta}^T_1, \ldots, \boldsymbol{\beta}^T_l, \boldsymbol{\rho}^T_1, \ldots, \boldsymbol{\rho}^T_l]^T, \tag{20}$$

where each of the l layers are a priori modeled as log-Gaussian random fields, but this is not used in this paper.

The seismic forward model

In Bayesian AVO inversion, the likelihood function can be defined as a pdf for the observed seismic data $\boldsymbol{d}_{obs}$ given a specific model parameter vector $\boldsymbol{m}_L$, denoted by the generic function $p(\boldsymbol{d}_{obs}|\boldsymbol{m}_L)$. The likelihood function describes how likely the observed data are for this specific model, and is coupled to the seismic forward modeling. The unconditioned pdf for the seismic data, denoted by the generic function $p(\boldsymbol{d}_{obs})$, is related to the likelihood function by

$$p(\boldsymbol{d}_{obs}) = \int p(\boldsymbol{d}_{obs}|\boldsymbol{m}_L)p(\boldsymbol{m}_L)\, d\boldsymbol{m}_L, \tag{21}$$

where $p(\boldsymbol{m}_L)$ is the prior model for the model parameters.

A discrete version of the reflectivity $c_{PP}(t,\theta)$ (see equation (9)) for a given time interval and a set of angles can be written

$$\boldsymbol{c} = \boldsymbol{A}\boldsymbol{m}'_L + \boldsymbol{e}_c, \tag{22}$$

where the matrix $\boldsymbol{A}$ is defined by the coefficients $\bar{a}_\alpha$, $\bar{a}_\beta$ and $\bar{a}_\rho$. The constant or slowly varying background model used to calculate the elements in $\boldsymbol{A}$ is now defined by the expectation of the prior model. The error term $\boldsymbol{e}_c$ is assumed to be independent of $\boldsymbol{m}'_L$ with Gaussian distribution

$$\boldsymbol{e}_c \sim \mathcal{N}_{n_c}(\boldsymbol{0}, \mathbf{\Sigma}_{e_c}), \tag{23}$$

where n_c is the number of reflection coefficients in a gather. The reflectivity $\boldsymbol{c}$ is then Gaussian

$$\boldsymbol{c} \sim \mathcal{N}_{n_c}(\boldsymbol{\mu}_c, \mathbf{\Sigma}_c) = \mathcal{N}_{n_c}(\boldsymbol{A}\boldsymbol{\mu}_{m'_L}, \boldsymbol{A}\mathbf{\Sigma}_{m'_L}\boldsymbol{A}^T + \mathbf{\Sigma}_{e_c}). \tag{24}$$

The seismic forward modeling of a seismic trace $\boldsymbol{d}_i$ (time trace for angle i) can be written as a convolution of a source wavelet $\boldsymbol{s}_i$ by the reflectivity $\boldsymbol{c}_i$

$$\boldsymbol{d}_i = \boldsymbol{s}_i \star \boldsymbol{c}_i, \tag{25}$$

or alternatively formulated as a matrix-vector multiplication

$$\boldsymbol{d}_i = \boldsymbol{S}_i\boldsymbol{c}_i, \tag{26}$$

where $\boldsymbol{S}_i$ represents the source wavelet for angle i. For all observed traces in an angle gather, we can write

$$\boldsymbol{d}_{obs} = \boldsymbol{S}\boldsymbol{c} + \boldsymbol{e}_d = \boldsymbol{S}(\boldsymbol{A}\boldsymbol{m}'_L + \boldsymbol{e}_c) + \boldsymbol{e}_d, \tag{27}$$

where $\boldsymbol{S}$ is a block-diagonal matrix of source wavelets $(\boldsymbol{S}_i, i = 1, \ldots, n_\theta)$. If we assume that the error term $\boldsymbol{e}_d$ is Gaussian

$$\boldsymbol{e}_d \sim \mathcal{N}_{n_d}(\boldsymbol{0}, \mathbf{\Sigma}_{e_d}), \tag{28}$$

then $\boldsymbol{d}_{obs}$ is Gaussian

$$\boldsymbol{d}_{obs} \sim \mathcal{N}_{n_d}(\boldsymbol{\mu}_{d_{obs}}, \mathbf{\Sigma}_{d_{obs}}) \tag{29}$$

where

$$\boldsymbol{\mu}_{d_{obs}} = \boldsymbol{S}\boldsymbol{A}\boldsymbol{\mu}_{m'_L} \tag{30}$$

$$\mathbf{\Sigma}_{d_{obs}} = \boldsymbol{S}(\boldsymbol{A}\mathbf{\Sigma}_{m'_L}\boldsymbol{A}^T + \mathbf{\Sigma}_{e_c})\boldsymbol{S}^T + \mathbf{\Sigma}_{e_d}. \tag{31}$$

The posterior model

Combination of equations (18) and (29), gives the simultaneous distribution

$$\begin{bmatrix} \boldsymbol{m}_L \\ \boldsymbol{d}_{obs} \end{bmatrix} \sim \mathcal{N}_{n_m+n_d}\left(\begin{bmatrix} \boldsymbol{\mu}_{m_L} \\ \boldsymbol{\mu}_{d_{obs}} \end{bmatrix}, \begin{bmatrix} \boldsymbol{\Sigma}_{m_L} & \boldsymbol{\Sigma}_{m_L,d_{obs}} \\ \boldsymbol{\Sigma}_{d_{obs},m_L} & \boldsymbol{\Sigma}_{d_{obs}} \end{bmatrix} \right) \tag{32}$$

where $\boldsymbol{\Sigma}_{d_{obs},m_L} = \boldsymbol{SA}\boldsymbol{\Sigma}_{m'_L,m_L}$ and $\boldsymbol{\Sigma}_{m_L,d_{obs}} = \boldsymbol{\Sigma}_{m_L,m'_L}\boldsymbol{A}^T\boldsymbol{S}^T$. The latter can be shown by

$$\begin{aligned} \boldsymbol{\Sigma}_{m_L,d_{obs}} &= \mathrm{Cov}\{\boldsymbol{m}_L, \boldsymbol{d}_{obs}\} \\ &= \mathrm{Cov}\{\boldsymbol{m}_L, \boldsymbol{SAm}'_L + \boldsymbol{Se}_c + \boldsymbol{e}_d\} \\ &= \mathrm{Cov}\{\boldsymbol{m}_L, \boldsymbol{SAm}'_L\} \\ &= \boldsymbol{\Sigma}_{m_L,m'_L}\boldsymbol{A}^T\boldsymbol{S}^T. \end{aligned} \tag{33}$$

The posterior distribution for the parameters $\boldsymbol{m}_L = (\ln\boldsymbol{\alpha}^T, \ln\boldsymbol{\beta}^T, \ln\boldsymbol{\rho}^T)^T$ given the seismic data $\boldsymbol{d}_{obs}$ is

$$\boldsymbol{m}_L|\boldsymbol{d}_{obs} \sim \mathcal{N}_{n_m}(\boldsymbol{\mu}_{m_L|d_{obs}}, \boldsymbol{\Sigma}_{m_L|d_{obs}}), \tag{34}$$

where

$$\begin{aligned} \boldsymbol{\mu}_{m_L|d_{obs}} &= \boldsymbol{\mu}_{m_L} + \boldsymbol{\Sigma}_{m_L,d_{obs}}\boldsymbol{\Sigma}^{-1}_{d_{obs}}(\boldsymbol{d}_{obs} - \boldsymbol{\mu}_{d_{obs}}) \\ &= \boldsymbol{\mu}_{m_L} + \boldsymbol{\Sigma}_{m_L,m'_L}\boldsymbol{A}^T\boldsymbol{S}^T\boldsymbol{\Sigma}^{-1}_{d_{obs}}(\boldsymbol{d}_{obs} - \boldsymbol{\mu}_{d_{obs}}), \end{aligned} \tag{35}$$

$$\begin{aligned} \boldsymbol{\Sigma}_{m_L|d_{obs}} &= \boldsymbol{\Sigma}_{m_L} - \boldsymbol{\Sigma}_{m_L,d_{obs}}\boldsymbol{\Sigma}^{-1}_{d_{obs}}\boldsymbol{\Sigma}_{d_{obs},m_L} \\ &= \boldsymbol{\Sigma}_{m_L} - \boldsymbol{\Sigma}_{m_L,m'_L}\boldsymbol{A}^T\boldsymbol{S}^T\boldsymbol{\Sigma}^{-1}_{d_{obs}}\boldsymbol{SA}\boldsymbol{\Sigma}_{m'_L,m_L}. \end{aligned} \tag{36}$$

The posterior distribution contains the complete solution of the inverse problem, including uncertainty. Possible, realistic solutions can be found by stochastic simulation from the posterior distribution: $\boldsymbol{m}_L^{(1)}, \boldsymbol{m}_L^{(2)}, \ldots$, and the corresponding solutions of the original parameters are obtained by the inverse transform

$$\boldsymbol{m}^{(i)} = \exp[\boldsymbol{m}_L^{(i)}]. \tag{37}$$

The MAP (maximum posterior distribution) solution of $\boldsymbol{m}_L$ is $\boldsymbol{\mu}_{m_L|d_{obs}}$, and the corresponding MAP solution of the original parameters can be obtained by

$$\widehat{\boldsymbol{m}}_{map} = \exp[\boldsymbol{\mu}_{m_L|d_{obs}}]. \tag{38}$$

The MAP solution is generally smoother than a single realization $\boldsymbol{m}^{(i)}$. In the case where the information content in the seismic data are only marginally with respect to the inversion parameters, the MAP solution will be defined mainly from the maximum of the prior distribution, which we have assumed to be smooth. A single realization, however, will be a possible solution with the full variability defined (mainly) from the prior distribution.

For a specific parameter, for example $\alpha_L(t)$, a prediction interval is given by

$$\mu_{\alpha_L|d_{obs}}(t) \pm x_{\frac{\epsilon}{2}}\sigma_{\alpha_L|d_{obs}}(t), \tag{39}$$

where x_ϵ is the ϵ-quantile in the standard Gaussian distribution, defined by $P(X > x_\epsilon) = \epsilon$. The probability that the true value of $\alpha_L(t)$ is in this interval is $1-\epsilon$. An approximative 0.95 interval for $\alpha(t)$ is given by $\exp[\mu_{\alpha_L|d_{obs}}(t) \pm 2\sigma_{\alpha_L|d_{obs}}(t)]$. Prediction intervals for parameters not contained in $\boldsymbol{m}$, for example Z_P, Z_S, or α/β, can easily be obtained by stochastic simulation.

A SYNTHETIC EXAMPLE

The algorithm is tested on two synthetic earth profiles (well A and B), shown in Figures 1 and 2. The two wells are simulated from a stationary prior distribution with constant expectation

$$\boldsymbol{\mu}(t) = \boldsymbol{\mu} = [\mu_\alpha, \mu_\beta, \mu_\rho]^T = [8.006, 7.313, 7.719]^T, \tag{40}$$

corresponding to the logarithm of 3000 m/s P-wave velocity, 1500 m/s S-wave velocity, and 2250 kg/m^3 density, and stationary covariance function on the form as in equation (13), where $\sigma^2_\alpha(t) = 0.0074$, $\sigma^2_\beta(t) = 0.0074$, and $\sigma^2_\rho(t) = 0.0024$. A second order exponential correlation function with range $d = 5$ ms is used for both wells, but the two wells have different correlation between $\ln\alpha$, $\ln\beta$ and $\ln\rho$: The logs in well A are uncorrelated, while the logs in well B have a relatively strong correlation (0.7).

Modeling test

The approximative reflection coefficient in equation (1) is widely accepted as a good approximation of the Zoeppritz equation in the weak contrast situation for moderate reflection angles. A further approximation is utilized in this inversion algorithm, where the coefficients $a_\alpha(t,\theta)$, $a_\beta(t,\theta)$ and $a_\rho(t,\theta)$ (equations (2) to (4)) are calculated from a constant or slowly varying prior known background model, defined by the expectation of the prior model (see equation (9)). The seismic forward modeling is performed by a convolution of the weak contrast reflectivity with source wavelets directly in the time-angle domain (see equations (25) and (27)). Real seismic data are recorded in the time-offset domain, and must be transformed to the time-angle domain prior to inversion.

Modeling tests of these approximations are shown in Figures 3 and 4 for well A and B, respectively. The CDP gathers to the left are calculated using weak contrast modeling directly in the time-angle domain. The coefficients $\bar{a}_\alpha(\theta)$, $\bar{a}_\beta(\theta)$ and $\bar{a}_\rho(\theta)$ are calculated from a constant background model defined in equation (40). The CDP gathers in the middle of the figures are produced by ray-tracing in the time-offset domain using the full Zoeppritz equation, and the gathers are then transformed to the time-angle domain. The gathers to the right show the differences between these two modeling methods. The relative squared data errors are only 0.0019 and 0.0027

for the two examples, which justifies the reflectivity approximation (9) and the offset to angle transformation for weak contrast models and moderate angles. This means that the error term $\boldsymbol{e}_c$ (see equations (22) and (23)) is negligible related to $\boldsymbol{e}_d$ (see equations (27) and (28)) in practical situations.

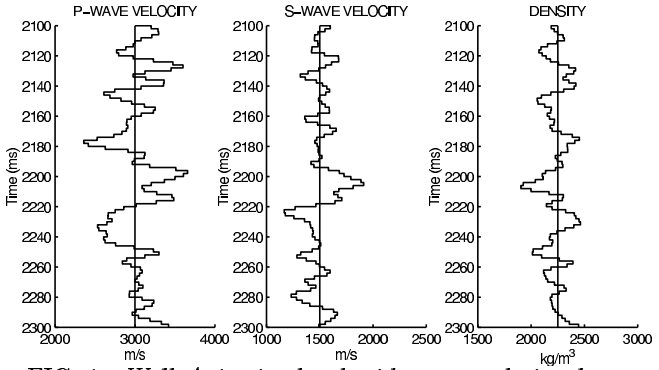

FIG. 1. *Well A is simulated with no correlation between the three logs (black lines). The constant background model is dotted.*

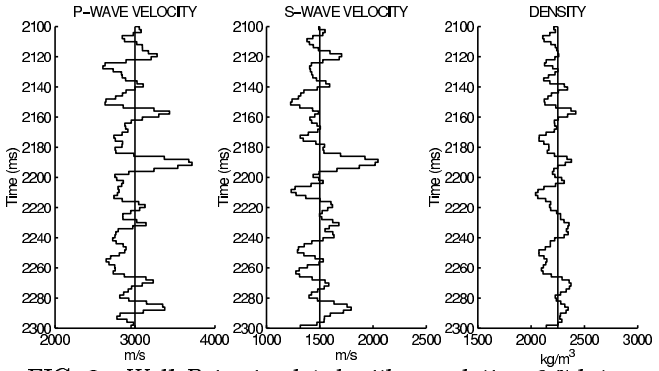

FIG. 2. *Well B is simulated with correlation 0.7 between each of the three logs (black lines). The constant background model is dotted.*

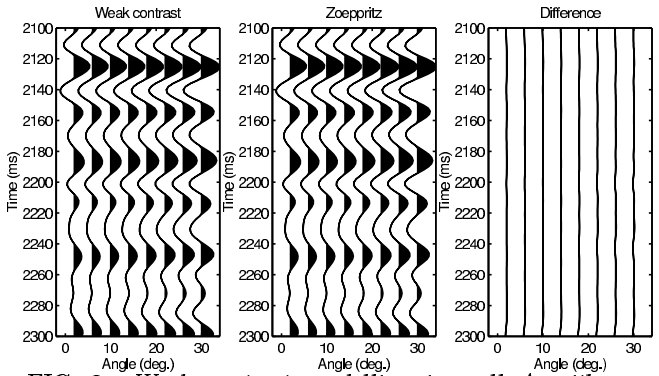

FIG. 3. *Weak contrast modelling in well A with constant background (left), raytracing with full Zoeppritz equation (middle) and residual (right).*

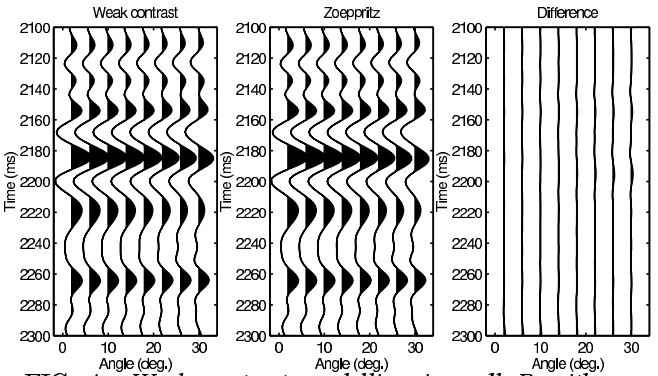

FIG. 4. *Weak contrast modelling in well B with constant background (left), raytracing with full Zoeppritz equation (middle) and residual (right).*

Inversion test

To obtain realistic synthetic seismic data sets for inversion tests, noise must be added. The noise is related to a long list of effects, such as complex wave propagation effects not included in the convolution model, background noise, measurement errors, and processing artifacts. A mixture of white and colored noise on the form

$$\boldsymbol{e}_d = \boldsymbol{e}_1 + \boldsymbol{S}\boldsymbol{e}_2 \tag{41}$$

was added to simulate these noise effects with different noise levels. The first term represents the white Gaussian noise where $\boldsymbol{e}_1 \sim \mathcal{N}_{n_d}(\boldsymbol{0}, \sigma_1^2 \boldsymbol{I})$. For each angle θ_i, the error term $\boldsymbol{e}_2(\theta_i)$ is also white Gaussian with variance σ_2^2, but this error term is colored by the source wavelet $\boldsymbol{S}$. Further, $\boldsymbol{e}_2$ is correlated between different angles by $\rho_\theta = \exp[-|\theta_i - \theta_j|/d_\theta]$, where $d_\theta = 20$ degrees is the correlation range. Noise gathers with four different levels were simulated with variances $\sigma_1^2 = \sigma_2^2 = 0.00005^2$, 0.008^2, 0.015^2, and 0.03^2. The CDP gathers for model A with noise are shown in Figure 5. The corresponding empirical signal to noise ratios (S/N) are 10^5, 15, 5 and 1.

The inversion results of dataset A with S/N ratio 10^5 are displayed in Figure 6, showing the MAP solution with a 95% prediction interval for P- and S-wave velocities, density, acoustic impedance, shear impedance and P- to S-wave velocity ratio. The three former are analytically obtainable, while the three latter are determined by stochastic simulation. The prior model applied is optimal in the sense that it is the same statistical model which was used to make the synthetic well logs and the corresponding seismic reference data. This includes the expectation and covariance functions of seismic parameters, the correlation range and the noise level in the seismic data. Also the correct source wavelet has been used (a Ricker wavelet with 25 Hz center frequency and normalized amplitude). The 95% interval of the prior model is shown in Figure 6 with dotted lines.

The inversion results of dataset A with S/N ratio 5 are displayed in Figure 7. The confidence regions are

much wider than in Figure 6, and the MAP solutions are smoother. Realizations from the posterior distribution for the data set with S/N ratio 5 are shown in Figure 8. These realizations have a higher, but more realistic, variability than the smooth MAP solution. Each of the realizations are possible solutions with this noise level. The large variation in these realizations intuitively explains the wide confidence regions.

A comparison of the 95% confidence regions for the prior and the posterior model makes a picture of the information content in the seismic prestack data, see Table 1. For model A, the seismic data provides most information about the acoustic impedance, the P- to S-wave velocity ratio, and the shear impedance for the case with S/N ratio 10^5, where the width of the confidence regions is reduced by 75 to 79 percent. In the case with an S/N ratio of 1, the seismic data provides most information about the acoustic impedance, the P-wave velocity and the P- to S-wave velocity ratio, but the intervals are only reduced by about 20 percent. In this case with strong noise, the seismic data provides practically no information about the S-wave velocity, the density and the shear impedance (3-4 percent reduction of the interval width).

In well A, the P-wave velocity, S-wave velocity and density are uncorrelated, but this is in most cases unrealistic. Well B is simulated with a strong correlation (0.7) between these three logs. The results in Table 2 shows that the confidence intervals for most parameters have been reduced more than in case A, but for the P- to S-wave velocity ratio the result is opposite.

S/N-ratio	α	β	ρ	Z_P	Z_S	α/β
10^5	71	66	58	79	75	78
15	37	20	12	46	26	39
5	33	11	8	40	11	30
1	21	3	4	25	3	17

TABLE 1. *Relative decrease in percent of the 95% interval from the prior model to the posterior model for selected parameters for model A.*

S/N-ratio	α	β	ρ	Z_P	Z_S	α/β
10^5	77	73	69	81	78	75
15	45	29	33	49	36	22
5	39	21	28	41	26	16
1	25	12	20	27	17	7

TABLE 2. *Relative decrease in percent of the 95% interval from the prior model to the posterior model for selected parameters for model B.*

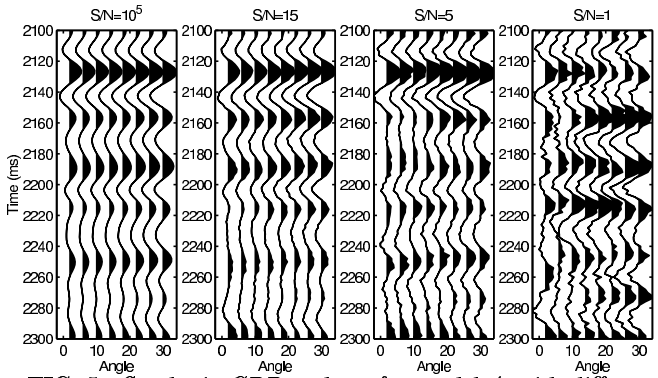

FIG. 5. *Synthetic CDP gathers for model A with different noise levels.*

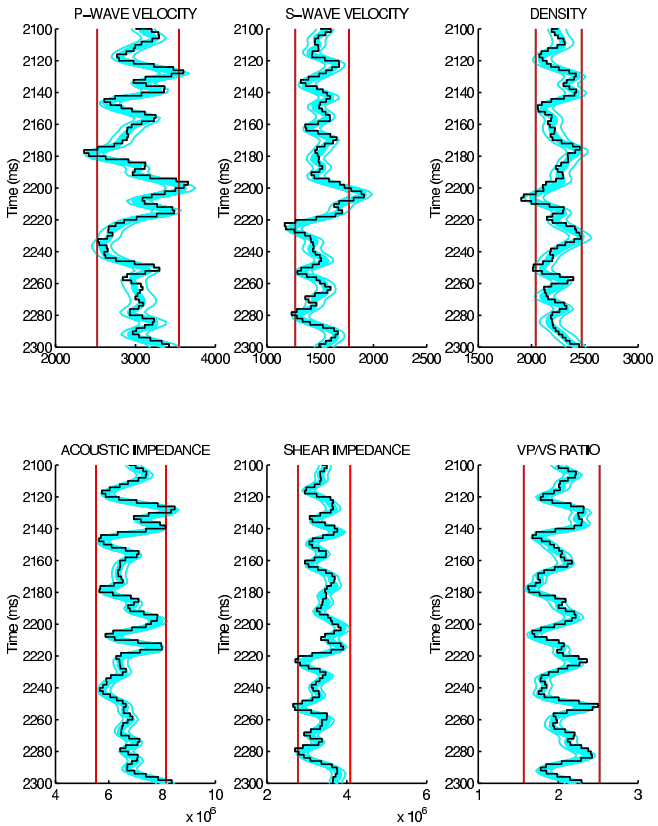

FIG. 6. *The MAP solution (thick blue line) of model A with S/N ratio 10^5 with 95% prediction interval (thin blue lines), the true earth profile (black), and 95% prior model interval (red dotted).*

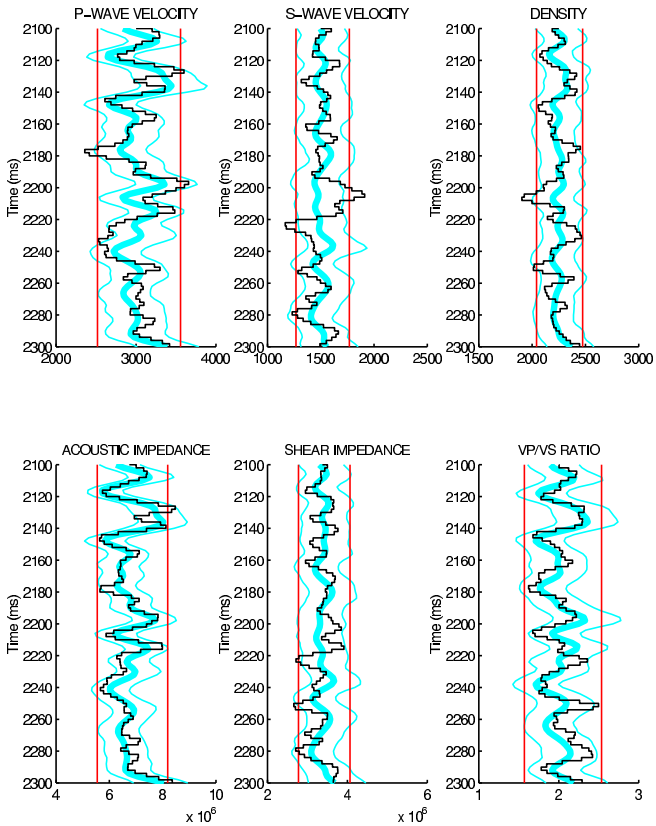

FIG. 7. *The MAP solution (thick blue line) of model A with S/N ratio 5 with 95% prediction interval (thin blue lines), the true earth profile (black), and 95% prior model interval (red dotted).*

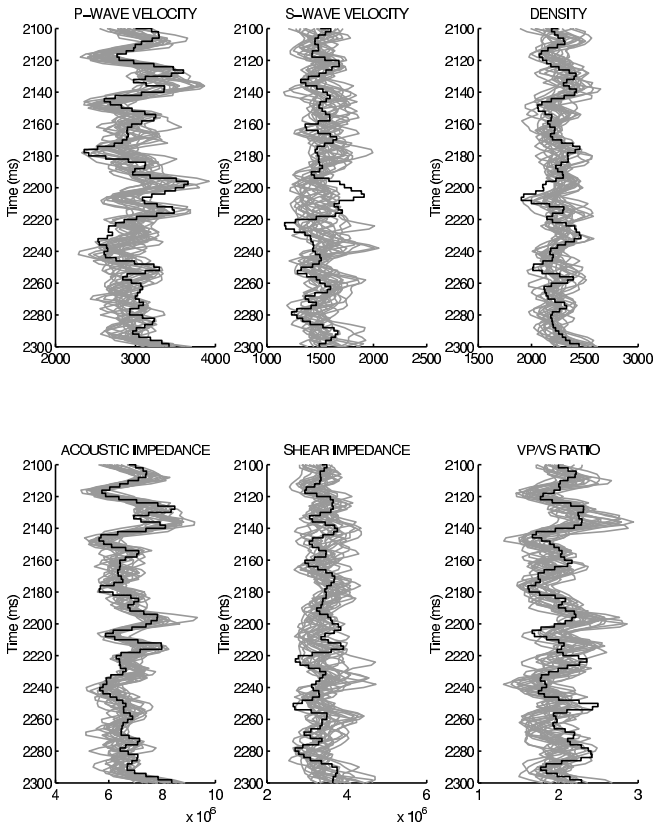

FIG. 8. *Realizations from the posterior distribution (gray lines) for model B with S/N ratio 5. The true earth profile is shown in black.*

INVERSION OF SLEIPNER DATA

The Sleipner Øst Field is located on the eastern side of the South Viking Graben in the Norwegian Block 15/9. The gas/condensate is trapped in a submarine-fan sandstone complex of the early Tertiary Ty Formation. The depth of the reservoir sand is in the range of 2270-2500 m sub-sea with the gas-water contact at 2415 m sub-sea. The reservoir underlies a thick shale package. The Ty Formation is composed of mainly clean sandstone interbedded with thin shale and siltstone layers. The base reservoir is a sand/chalk interface (Top Shetland Formation).

A rectangular part of the total seismic survey, defined from inlines 1411 to 1751, and crosslines 1225 to 1400, is used in this inversion test. The inversion test area covers 9.3 km^2, representing 12 percent of the total survey. The seismic data were processed by a contractor company, with the processing sequence shown in Table 3. Stack section of inline 1627 are shown in Figure 9, where the strong continuous reflector appearing between 2350 and 2500 ms is the Top Shetland horizon (base reservoir).

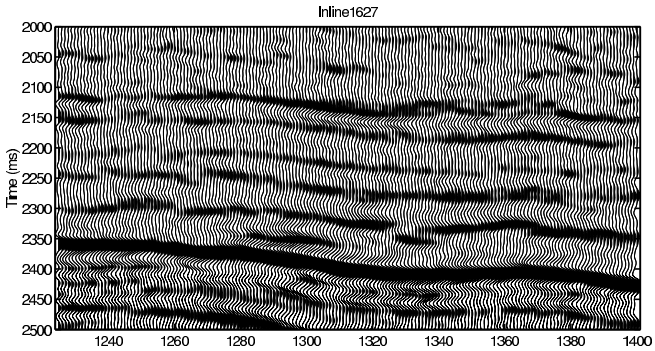

FIG. 9. *Stack section of inline 1627.*

1. SEGD read and data editing
2. Navigation merge
3. Gun, cable and filter delay correction (-38.6 ms)
4. Deterministic zero phasing
5. Lowcut filter 6Hz
6. Gaincorrection t^2
7. Tidal correction
8. Swell noise and interference attenuation
9. Forward $\tau - p$ transformation
10. Predicted deconvolution 64/300 ms gap/operator
11. Inverse $\tau - p$ transformation
12. Old velocity input
13. NMO
14. k-filter spatial resampling
15. CMPs to 75 m trace spacing
16. Sort to 39 offsetvolumes, 50% xline binning
17. $f - x$-trace interpolation, hole-filling
18. Static correction
19. DMO, reduction to 19 offsets
20. Prestack time-migration with minimum velocity
21. Inverse NMO with old velocities
22. New velocity picking
23. NMO with new velocities
24. Transform to time-angle by ray-tracing

TABLE 3. *Processing sequence*

Prior model estimation

A well is located at the inline, crossline coordinates (1627,1291). The well logs are displayed as function of depth in Figure 10, where the impedance logs and the P- to S-wave velocity ratio log are calculated from the P-wave velocity, S-wave velocity and density logs.

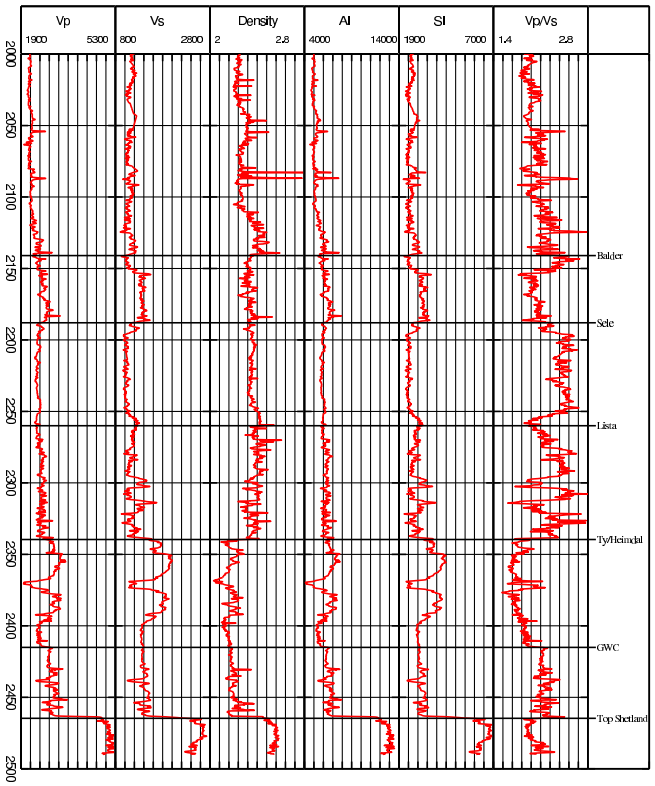

FIG. 10. *The well logs plotted in the depth interval 2000-2500 m.*

Top reservoir is characterized by an increase in P-wave velocity (20%), a large increase in S-wave velocity (60%), and a small decrease in density (-8%). The usually well determined acoustic impedance has only a minor increase from the shale to the gas sand (12%). Increase in the S-wave velocity may therefore be a better indicator for top reservoir.

Base reservoir is well defined on a seismic stack by the strong Top Shetland reflector. In the well, the P-wave velocity increases from about 3000 m/s in the sand reservoir to about 5000 m/s in the Top Shetland chalk formation, the S-wave velocity increases from about 1400 to 2600 m/s, and the density increases from 2200 to 2550 kg/m^3, which gives a reflection coefficient of about 0.3. As the inversion algorithm is based on a weak contrast assumption, the inversion window is defined as a 250 ms window ending 32 ms above Top Shetland (a half wavelet). At the well, the inversion window is 2100 to 2350 ms.

The P-wave velocity, S-wave velocity, and density are assumed to be adequately modeled as a log-Gaussian ran-

dom field. That implies that the logarithm of these parameters must be close to Gaussian. QQ-plots of the well-logs in the time interval 2100-2350 ms are shown in Figure 11, which we consider to be acceptable.

We assume a stationary covariance function on the form $\boldsymbol{\Sigma}(\tau) = \boldsymbol{\Sigma}_0 \rho_S(\tau)$ for the prior model of $\boldsymbol{m}_L$. From the well logs, estimates of the elements in $\boldsymbol{\Sigma}_0$ are obtained by standard estimators. The estimated variances for $\ln \alpha$, $\ln \beta$ and $\ln \rho$ are $\widehat{\sigma_\alpha^2} = 0.0037$, $\widehat{\sigma_\beta^2} = 0.0116$, and $\widehat{\sigma_\rho^2} = 0.0004$, and the estimated correlation coefficients are $\widehat{\rho_{\alpha,\beta}} = 0.65$, $\widehat{\rho_{\alpha,\rho}} = 0.11$, $\widehat{\rho_{\beta,\rho}} = -0.07$.

Empirical temporal correlation functions from the well logs are shown in Figure 12 (stars). The empirical correlation function is represented by $\rho_S(\tau; d_1, d_2) = \frac{1}{2}\rho_{S_1}(\tau; d_1) + \frac{1}{2}\rho_{S_2}(\tau; d_2)$, where $\rho_{S_1}(\tau; d_1)$ is an exponential second order correlation function with range $d_1 = 1.8$ ms, and $\rho_{S_2}(\tau; d_2)$ is a normalized second derivative of an exponential second order correlation function with range $d_2 = 9$ ms.

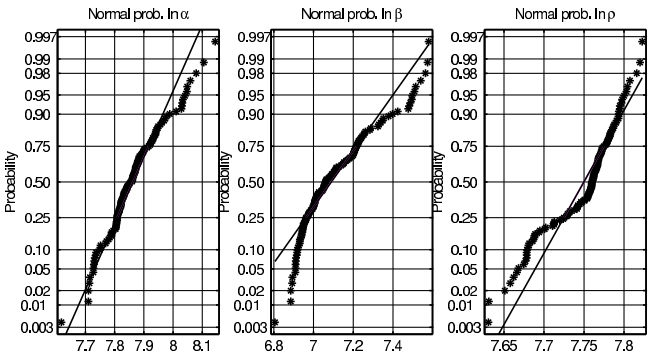

FIG. 11. *QQ-plot of the logarithm of the P-wave velocity (left), S-wave velocity (middle), and density (right).*

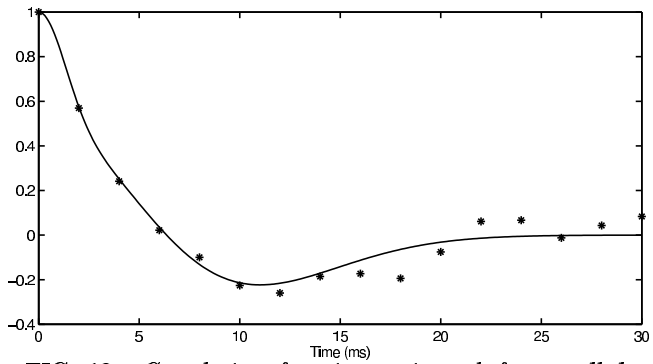

FIG. 12. *Correlation function estimated from well logs (stars), and a correlation function derived from two exponential second order correlation functions.*

Estimation of source wavelets and noise covariance

The last step before inversion is to estimate source wavelets and the seismic data noise covariance matrix from calculated well-log reflectivity $\boldsymbol{C}$ and the CDP gather in the well position $\boldsymbol{d}_{obs}$. Angle-dependent source wavelets are estimated by solving the least-squares problem $\hat{\boldsymbol{s}} = (\boldsymbol{C}^T\boldsymbol{C})^{-1}\boldsymbol{C}^T\boldsymbol{d}_{obs}$, see Figure 13. The real CDP gather in the well position and the corresponding synthetic gather $\boldsymbol{d}_{syn} = \boldsymbol{C}\hat{\boldsymbol{s}}$ are shown in Figure 14.

The misfit between $\boldsymbol{d}_{obs}$ and $\boldsymbol{d}_{syn}$ can partly be explained by the seismic noise $\boldsymbol{e}_d$, and partly by errors in the well log reflectivity $\boldsymbol{e}_w$. The latter is obviously related to measurement errors, but errors related to the depth to time conversion of the well logs and uncertainty in well position may be more serious. A common procedure in source estimation and well tie analysis is to slightly shift, stretch and squeeze the well logs in time after the depth to time conversion without changing the log values. In this case, such correction of the time axis is performed by visual inspection of the seismic gathers, but it is reasonable to assume that there are small remaining time shift errors which cause considerable data misfit.

The seismic data noise is assumed to be a mixture of white and colored noise on the form $\boldsymbol{e}_d = \boldsymbol{e}_1 + \boldsymbol{S}\boldsymbol{e}_2$. We find $\widehat{\sigma_1^2} = 0.0114$ and $\widehat{\sigma_2^2} = 0.0004$, and the estimated correlation range for $\boldsymbol{e}_2$ is $\hat{d}_\theta = 20$ degrees.

Ideally, more than one well should be used in source and noise covariance estimation to reduce uncertainty in the estimation. Also more sophisticated methods for wavelet and noise estimation can be discussed, but this is beyond the scope of this paper.

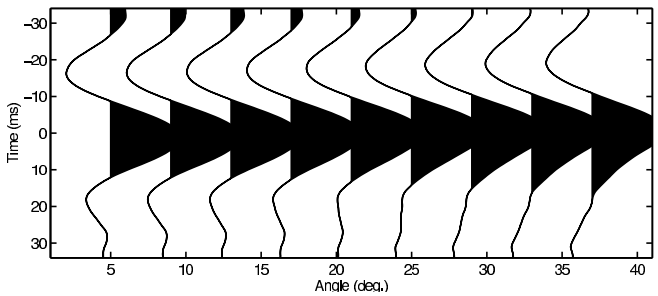

FIG. 13. *Estimated source wavelets at reservoir level.*

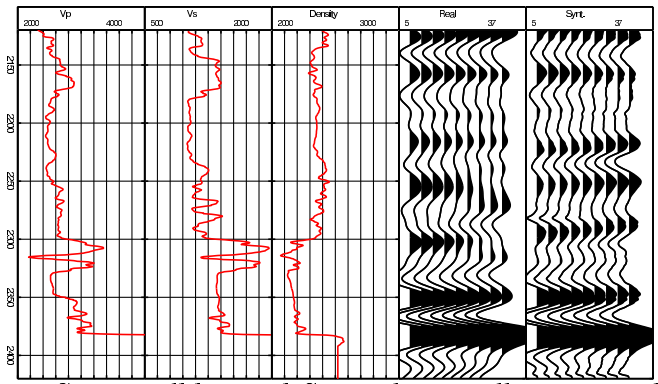

FIG. 14. *Well logs, real CDP gather in well position, and synthetic CDP gather calculated by convolution of the well log reflectivity and the estimated source wavelets.*

Inversion results

The inversion results in the well position are displayed in Figure 15, showing the MAP solutions and 95% prediction intervals. With the estimated noise level in this data set, the prediction intervals are only marginally reduced compared to the prior model. The acoustic impedance and the P-wave velocity are the best determined parameters, but the prediction intervals are only reduced by 31 and 27 percent, respectively. The prediction intervals for the P- to S-wave velocity ratio, the shear impedance and the S-wave velocity are reduced by about 15 percent, while the interval for the density is reduced by only 5 percent. Top reservoir is located at 2300 ms, and is characterized by an increase in both P- and S-wave velocity. This increase in the two velocities is seen in the inversion results, but the strong oscillations in the upper part of the reservoir (2300-2330 ms) are only partly retrieved by the smooth MAP solution.

The MAP solutions of inline 1627 are shown in Figure 16. The bottom of the inversion window is shown by a thick black line 32 ms above the Top Shetland horizon. The well logs are plotted for control, and show a good agreement with the inversion results.

Time slices (2314 ms) of the P- and S-wave velocities are shown in Figure 17. The intersection of the top reservoir interpreted from stacked data is shown by a black line, and show a high agreement with the inversion results. At some places, minor modifications of the stack interpretation may be considered.

The inversion algorithm is fast. After a start-up time, the inversion of the 3-D test cube was finished in one hour on a single CPU machine (1000 CDP gathers/min.). The algorithm is suitable for parallelization. On a 8 CPU parallel machine, the whole survey (77.5 km^2) could be inverted in approximately one hour.

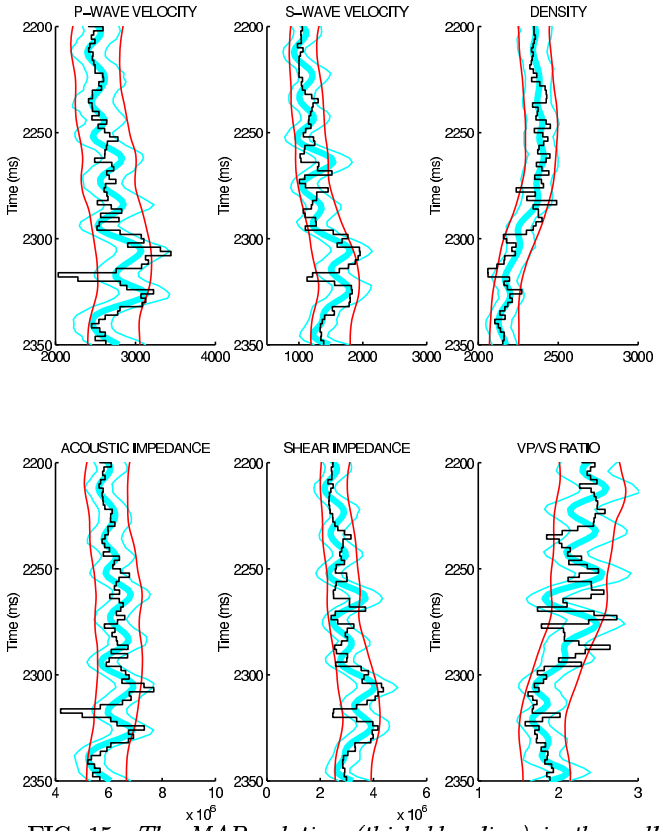

FIG. 15. *The MAP solution (thick blue line) in the well position with 95% prediction interval (thin blue lines), the well log (black), and 95% prior model interval (red dotted).*

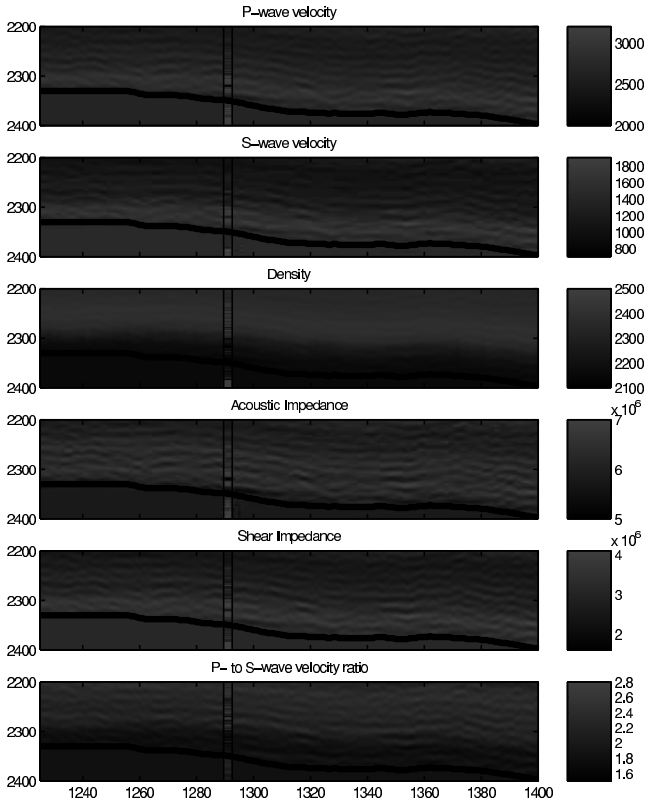

FIG. 16. *MAP solution of inline 1627.*

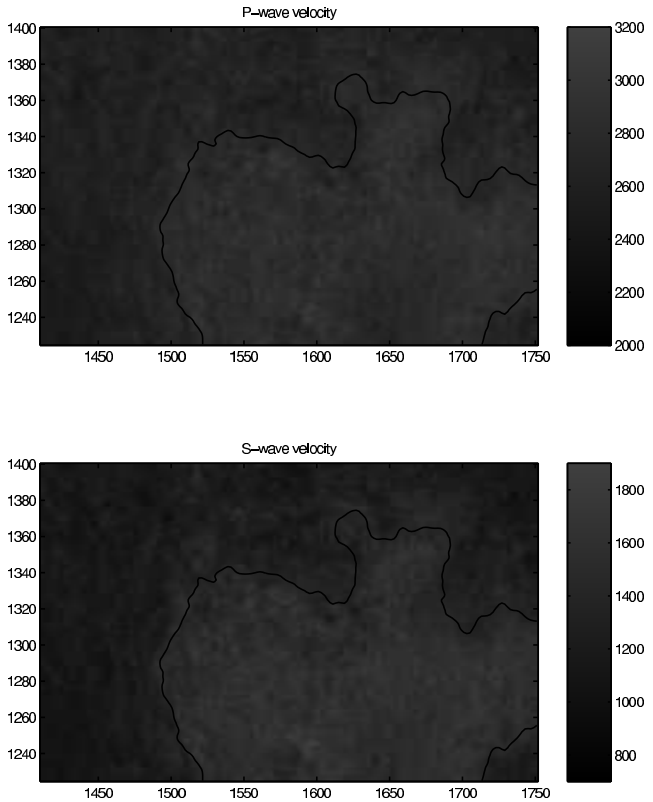

FIG. 17. *Time slice of MAP solution. The interpreted top reservoir is shown by black line.*

DISCUSSION AND CONCLUSIONS

We have developed a Bayesian AVO inversion method where the uncertainty in the inverted parameters is an integrated part of the solution. The inversion algorithm is based on a time continuous weak contrast model. The model parameters are represented by spatial log-Gaussian fields, and derivative Gaussian fields are involved to couple the absolute values of the parameters to the contrast model needed in the reflectivity calculation. The solution of the AVO inversion is given on an analytical form. The inversion algorithm is fast and have been tested on synthetic gathers and a 3-D real dataset from the Sleipner Field.

AVO inversion is an ill-posed problem. Weak noise have a dramatic effect on the uncertainty of the predicted parameters. Acoustic impedance is the best determined and most robust parameter, while AVO inversion provides practically no information about density in all realistic cases. The resolution of the different parameters depends on the dependency between the parameters and the statistical properties of the noise.

ACKNOWLEDGMENTS

We thank the Sleipner licence (Statoil, Exxon/Mobil, Norsk Hydro and TotalFinaElf) for permission to publish this paper.

REFERENCES

Abrahamsen, P., A review of gaussian random fields and correlation functions:, Technical report, Norwegian Computing Center, P.O. Box 114, Blindern, N-0314 Oslo, Norway, 1997.

Aki, K., and Richards, P. G., 1980, Quantitative seismology: W.H. Freeman and Co.

Buland, A., Landrø, M., Andersen, M., and Dahl, T., 1996, AVO inversion of Troll Field data: Geophysics, **61**, 1589–1602.

Christakos, G., 1992, Random field models in earth sciences: Academic Press Inc., San Diego.

Dahl, T., and Ursin, B., 1991, Parameter estimation in a one-dimensional anelastic medium: J. Geophys. Res., **96**, 20217–20233.

Duijndam, A. J. W., 1988a, Bayesian estimation in seismic inversion. Part i: Principles: Geophys. Prosp., **36**, 878–898.

—— 1988b, Bayesian estimation in seismic inversion. Part ii: Uncertainty analysis: Geophys. Prosp., **36**, 899–918.

Eide, A. L., Omre, H., and Ursin, B., Uncertainty in seismic inversion for reservoir characterization:, Technical Report Statistics No. 10/1999, NTNU, Dept. of Mathematical Sciences, N-7034 Trondheim, Norway, 1999.

Hampson, D., and Russell, B., 1990, AVO inversion: Theory and practice: 60th Ann. Internat. Mtg., Soc. Expl. Geophys., Expanded Abstracts, 1456–1458.

Lörtzer, G. J. M., and Berkhout, A. J., 1993, Linearized AVO inversion of multicomponent seismic data, *in* Castagna, J., and Backus, M., Eds., Offset-dependent reflectivity - Theory and practice of AVO analysis: Soc. Expl. Geophys., 317–332.

Mosegaard, K., and Tarantola, A., 1995, Monte Carlo sampling of solutions to inverse problems: J. Geophys. Res., **100**, 12431–12447.

Mosegaard, K., 1998, Resolution analysis of general inverse problems through inverse Monte Carlo sampling: Inverse problems, **14**, 405–426.

Sen, M. K., and Stoffa, P. L., 1996, Bayesian inference, Gibbs' sampler and uncertainty estimation in geophysical inversion: Geophys. Prosp., **44**, 313–350.

Tarantola, A., and Valette, B., 1982a, Inverse problems = quest for information: J. Geophys., **50**, 159–170.

Tarantola, A., 1987, Inverse problem theory: Elsevier Science Publ. Co. Inc.